Geophys. J. R. astr. Soc. (186) **85**, 523–541

Numerical study of high Rayleigh number convection in a medium with depth-dependent viscosity

Michael Gurnis and Geoffrey F. Davies *Research School of Earth Sciences, Australian National University, GPO Box 4, Canberra, ACT 2601, Australia*

Accepted 1985 October 19. Received 1985 May 8; in original form 1984 October 2

Summary. The equations of motion are solved numerically for a Boussinesq fluid with infinite Prandtl number in a square 2-D box where the viscosity increases with depth. Three heating modes are employed: bottom heating, internal heating, and half bottom and half internal heating. In all cases the boundaries are free slip. The range of Rayleigh numbers employed is 10^4–10^7. The viscosity increases as $10^{\beta(1-y)}$, where y is distance measured from the bottom upwards and β is a free parameter. In the bottom heated cases, the convective velocities slow near the bottom and result in a large temperature drop between the bottom boundary and interior compared with the top boundary and the interior. This results in increased buoyancy in the ascending limb. In the internally heated case, the flow in the top half of the box resembles Rayleigh–Bènard convection and in the bottom half it approaches a conductive thermal regime for β greater than about 2. In this case the top surface heat flux decays from ascending to descending limb and the ascending and descending limbs become more equal in their buoyancy. Increasing β decreases the efficiency of heat transport, but has little effect on the exponents of Nu-Ra and Pe-Ra relations. There is a larger decrease in heat transport efficiency for a given β in the bottom heated case compared to the internally heated case.

Key words: mantle convection, mantle viscosity

1 Introduction

The concept of whole mantle convection is getting widespread attention because of its ability to reconcile diverse geophysical and isotopic observations (Hager & O'Connell 1979; Creager & Jordan 1984; Davies 1984). It must be emphasized that the form of mantle convection is controversial and that the whole mantle convection scenario is only a working hypothesis. For example, in global flow models with observed plate kinematics prescribed, flow penetrating into the lower mantle is consistent with the observed dips of Benioff zones

while flow confined only to the upper mantle is not (Hager & O'Connell 1979). Moreover, seismic velocity anomalies have been detected to 1000 km depth beneath the Sea of Okhotsk and are consistent with the Kuril–Kamchatka slap penetrating deep into the lower mantle (Jordan 1977; Creager & Jordan 1984). Despite these geophysical observations which seem to suggest that the flow associated with plates extends deep into the mantle, there are some geochemical observations not obviously in accord with the model: the 'age' of some oceanic island basalts (OIB) sources, which are up to billions of years as revealed by ^{129}Xe isotopic ratios (Allègre *et al.* 1983) and the continuing flux of 'primitive' ^{3}He from the mantle (Lupton & Craig 1975). In order to reconcile these diverse observations, Davies (1984) has proposed a model of mantle dynamics with the following attributes. First, flow associated with plates extends through the whole mantle. Second, the heterogeneous signatures of OIB as revealed by Pb, Sr, and Nd isotopes (Allègre *et al.* 1980; Hofmann 1984) are explained by the presence of heterogeneities dispersed through the convecting mantle. And third, the apparently low relative velocity of hot-spots (Molnar & Francheteau 1975) and the persistence of some heterogeneities for 4.4 Byr is consistent with a moderate increase in viscosity with depth through the mantle.

The one to two orders of magnitude increase in viscosity hypothesized by Davies (1984), is unlikely to be inconsistent with the observed 'uniform viscosity' of the whole mantle as inferred from studies of post-glacial rebound (Cathles 1975; Peltier & Andrews 1976). With the exponential viscosity distribution assumed for this study, most of the viscosity through the layer is fairly uniform and most variation occurs through the bottom third. It is difficult to assess the uncertainty of post-glacial rebound studies because the errors are not explicitly studied. What is really needed is a systematic study of many viscosity distributions to see if the type of distributions presumed here and in Davies (1984) are either inconsistent or unresolvable with present observations and techniques.

Recently, however, Hager (1984) has made an entirely independent estimate of the relative variation of viscosity with depth on the basis of the observed geoid anomalies over oceanic trenches. The positive geoid anomalies seem to require that the viscosity increase by a factor of 30 or more through the whole mantle (assuming that the subducted slabs extend into the lower mantle).

Convection extending through the whole mantle and with a moderate increase in mantle viscosity with depth is a good working hypothesis which needs further exploration. The purpose of this paper is systematically to explore the effect that depth-dependent viscosity has on thermal convection at high Rayleigh numbers. The models presented here are *not* intended to be realistic models of mantle convection – the purpose of the calculations is to instruct us in the very basic features of convection in a medium with depth-dependent viscosity so that, in realistic models, we will fully understand what effect the depth dependence has. The approach being taken in this paper is to emphasize very basic and robust phenomena: qualitative features of the fluid flows in terms of the temperature and velocity fields.

There have been a few numerical studies of convection in a layer with depth-dependent viscosity. Torrance and Turcotte (1971a) presented three runs with progressively larger viscosity increases at low Rayleigh number. Houston & De Bremaeker (1975) also considered a few cases with just depth dependence. Davies (1977) systematically studied a two-layer geometry with a thin low-viscosity layer overlying a high-viscosity region at the onset of convective instability. Londe & Davies (1985) presented numerical boundary layer calculations at high Rayleigh numbers (up to 10^9) with bottom heating. There have also been other studies where depth dependence has been considered as just a single parameter in multi-parameter viscosity relations: Torrance & Turcotte (1971b), and Christensen (1983,

1984). Despite these studies, the basic features of convection in a depth-dependent medium have not been documented.

2 Governing equations and numerical solution

The equations of motion are solved numerically in a 2-D square box and the Boussinesq approximation is used. All four sides of the box are free-slip (i.e. zero tangential stress). The top surface is held at a constant temperature, while the bottom surface can be either held at a constant temperature or at a constant heat flux. Uniform internal heat generation is also possible.

Neglecting inertial terms, the momentum equation (e.g. Landau & Lifshitz 1959) with buoyancy is written in tensor notation as

$$\frac{\partial \sigma_{ij}}{\partial x_j'} - \rho \alpha T' g \lambda_i = 0 \tag{1}$$

where $\lambda = (0, -1)$ and is the unit vector pointing in the direction of gravity, g is the magnitude of the gravitational acceleration, ρ is the density, α is the coefficient of thermal expansion, T' is the temperature, and σ_{ij} is the stress tensor:

$$\sigma_{ij} = -p\delta_{ij} + \tau_{ij} \tag{2}$$

where p is the pressure, δ_{ij} is the Kronecker delta, and τ_{ij} is the deviatoric stress. In the problem considered in this paper, the viscosity is not spatially constant and the deviatoric stress is written as

$$\tau_{ij} = 2\eta' \left(e_{ij} - \frac{1}{3} e_{ii} \delta_{ij} \right) \tag{3}$$

where

$$e_{ij} = \frac{1}{2} \left(\frac{\partial u_i'}{\partial x_j'} + \frac{\partial u_j'}{\partial x_i'} \right) . \tag{4}$$

In (3), η' is the dynamic viscosity and depends only on position. The equations will be non-dimensionalized as

$$\begin{aligned} (x, y) &= (x', y')/D' \\ (u, v) &= (u', v')/V_0' \\ T &= T'/\Delta T' \\ \eta &= \eta'/\eta_0' \end{aligned} \tag{5}$$

where D' is the depth of the box, $\Delta T'$ a temperature scale defined below, η_0' is the dynamic viscosity at the top surface, and

$$V_0' = \frac{\rho g \alpha \Delta T' D'^2}{\eta'} . \tag{6}$$

The three heating modes employed in this study are: (i) all heat entering the bottom with a constant bottom temperature, (ii) all heat generated internally with a constant bottom heat flux, and (iii) half bottom heated and half internally heated with a constant bottom

heat flux. $\Delta T'$ is defined to accommodate these cases:

$$\Delta T' = T_b' - T_t' \tag{7a}$$

or

$$\Delta T' = QD/K \tag{7b}$$

where T_b' and T_t' are the bottom and top temperatures, respectively, K the thermal conductivity, and Q is defined as

$$Q = q_b + HD \tag{8}$$

where q_b is the heat flux at the bottom boundary and H is the rate of internal heat production per unit volume.

With this dimensionalizing scheme and with $(x_1, x_2) = (x, y)$ and $(u_1, u_2) = (u, v)$, we substitute (2), (3) and (4) into (1) and take the curl to eliminate the pressure (Torrance & Turcotte 1971a):

$$\nabla^2(\eta\omega) = -\frac{\partial T}{\partial x} - 2\left[\frac{\partial^2\eta}{\partial x^2}\frac{\partial u}{\partial y} - \frac{\partial^2\eta}{\partial y^2}\frac{\partial v}{\partial x} + \frac{\partial^2\eta}{\partial x\partial y}\left(\frac{\partial v}{\partial y} - \frac{\partial u}{\partial x}\right)\right] \tag{9}$$

where x and y are the horizontal and vertical directions (y measured from the bottom upwards and x from the left), u and v the horizontal and vertical velocities and ω the vorticity, defined as

$$\omega = \omega_{12} = \left(\frac{\partial v}{\partial x} - \frac{\partial u}{\partial y}\right). \tag{10}$$

In this study we have only considered vertical variations in viscosity, so that $\partial\eta/\partial x = 0$ and (9) becomes

$$\nabla^2(\eta\omega) = -\frac{\partial T}{\partial x} + 2\frac{\partial^2\eta}{\partial y^2}\frac{\partial v}{\partial x}. \tag{11}$$

The viscosity is assumed to exponentially increase with depth as

$$\eta = 10^{\beta(1-y)} = \exp\left[C(1-y)\right] \tag{12}$$

which is similar to the form used by Torrance & Turcotte (1971a) and Londe & Davies (1985). It must be emphasized that the exponential viscosity distribution was chosen solely because the solutions to this flow problem can be solved accurately and rapidly. The models are run for integer values of β, so that from (12) it is immediately clear that, for example, $\beta = 2$ means a difference of 100 between the top and bottom of the box. Substituting (12) into (11) we have

$$\nabla^2(\eta\omega) = -\frac{\partial T}{\partial x} - 2C^2\eta\frac{\partial^2\psi}{\partial x^2} \tag{13}$$

where ψ is the stream function, and is defined in the usual way as

$$u = \frac{\partial\psi}{\partial y} \quad v = -\frac{\partial\psi}{\partial x}. \tag{14}$$

It follows that

$$\nabla^2\psi = -\omega. \tag{15}$$

In this problem, the viscosity variations do not enter into the heat equation, so that it can be written as (cf. Landau & Lifshitz 1959):

$$\frac{\partial T}{\partial t} + \frac{\partial}{\partial x}(uT) + \frac{\partial}{\partial y}(vT) = \frac{1}{\mathrm{Ra}}(\nabla^2 T + \mu) \tag{16}$$

where t is time, Ra is a Rayleigh number and μ is the ratio of internal to total heat production and these are defined (returning to dimensional variables) as

$$\mathrm{Ra} = \frac{\rho g \alpha D^3 \Delta T}{\kappa \eta_0} \tag{17}$$

$$\mu = \frac{HD^2}{K \Delta T}. \tag{18}$$

In this study, the choice of η_0 in (17) is important. Many definitions of Ra are possible. Because any estimate of mantle viscosity will be biased toward upper mantle values, defining Ra in terms of the surface viscosity is reasonable. Estimates made for the mantle Ra can be directly compared to values calculated with equation (17). With the different heating modes and two definitions of the temperature difference, ΔT, we define two corresponding Rayleigh numbers:

$$\mathrm{Ra_T} = \frac{\rho g \alpha D^3 (T_b - T_t)}{\kappa \eta_0} \tag{19}$$

$$\mathrm{Ra_q} = \frac{\rho g \alpha D^4 Q}{K \kappa \eta_0}. \tag{20}$$

The results of the numerical simulations will be discussed with certain average quantities. Parameters that are horizontally averaged across a row of mesh points will be denoted as, for example $\langle U_{\mathrm{TOP}} \rangle$, i.e. the horizontally averaged horizontal velocity across the top boundary. Quantities that are averaged at every mesh point are denoted as $\bar{T}$, i.e. the average temperature. The average heat transported by the flow is normalized as

$$\mathrm{Nu} = q/q_c \tag{21}$$

which is the Nusselt number, q is the average heat flow across the top boundary, and q_c is the heat transported by conduction assuming there is no convection. The velocities are normalized as

$$\mathrm{Pe} = \frac{D \langle U_{\mathrm{TOP}} \rangle}{\kappa} \tag{22}$$

which is the Peclet number.

2.1 NUMERICAL SOLUTION

The equations are solved by standard finite difference techniques and we follow the algorithms of Lux (1978) as modified by Davies (1986) and below. The momentum equation is written as two Poisson equations (equations 13 and 15) and the algorithm described by Sweet (1974) is used successively to solve each one. The alternating direction implicit (ADI) method with upwind differencing is used to solve the energy equation. The

second term on the right side of (13), arising from the viscosity variations, is not known *a priori*, and was found by iteration, as follows. We define

$$\xi_{ij} = \nabla^2 (\eta \omega_{ij}). \tag{23}$$

The algorithm consists of the following sequence of operations:

(1) $\xi_{ij}^{n+1} = (1-\delta)\,\xi_{ij}^{n} + \delta\, C^2\, \eta(\psi_{i,j+2}^{n} + \psi_{i,j}^{n} - 2\,\psi_{i,j+1}^{n})$

where n is an iteration counter,

(2) $\epsilon = \max \left| \xi_{i,j}^{n+1} - \xi_{i,j}^{n} \right|$ all i, j,

(3) the Poisson equation of (19) is solved for ω,

(4) the Poisson equation (15) is solved for ψ,

(5) if $\epsilon > \epsilon_0$ return to step (1) and carry out the sequence again. If $\epsilon < \epsilon_0$ go on to solve the heat equation.

The quantity ξ converged quickly at every time step, and in general required no more than two passes through steps (1)–(5), except for the first two time steps when the calculation starts, when n up to 5 is required. A $\delta = 0.5$ was used for all calculations except for the few runs at $\beta = 3$, when a δ of 0.3 was used. An ϵ_0 of 3×10^{-5} was used in all cases.

2.2 NUMERICAL ACCURACY

In high Rayleigh number convection, the thermal boundary layers become quite thin (cf. McKenzie, Roberts & Weiss 1974) and therefore a fine numerical mesh is needed to resolve the thermal structure. Moore & Weiss (1973) suggest, for example, that at least three mesh points spanning the thermal boundary layers are needed for calculations accurate to within 1 per cent. For the new calculations presented in this paper (i.e. those with depth-dependent viscosity) there were at least three mesh points across thermal boundary layers and Nusselt numbers and other quantities have errors of 5 per cent or less; this was determined by running the code with the same parameters, but different grid sizes. However, those cases with constant viscosity, which were repeats from McKenzie *et al.* (1974) and Jarvis & Peltier (1982), were of less accuracy in that some cases only had one to two mesh spacings spanning the thermal boundary layers. This was only done to save computer time. We should emphasize, however, that despite the fairly coarse grids, we were able to duplicate the Nu values presented by Jarvis & Peltier (1982) as will be demonstrated in the next section.

Table 1. Summary of models with constant bottom temperature.

Model	Ra_T	Mesh points	β	Initial condition $\bar{T}$ or model	Flow† concentrated	Total flow time	$\bar{T}$ final	Nu	$\langle U_{TOP} \rangle$	$\bar{U}$	$\langle U_{BOT} \rangle / \langle U_{TOP} \rangle$
B1	10^4	31	0	0.5	na	2.8×10^3	0.500	4.966	4.22×10^{-3}	2.47×10^{-3}	1.000
B2	10^4	31	1	B1	?	1.5×10^3	0.444	2.940	2.18×10^{-3}	9.27×10^{-4}	0.468
B3	10^5	31	0	0.25	na	1.0×10^4	0.490	10.66	2.03×10^{-3}	1.11×10^{-3}	1.001
B4	10^5	31	0	0.5	na	2.7×10^3	0.511	10.93	2.02×10^{-3}	1.11×10^{-3}	1.009
B5	10^5	31	0	0.75	na	1.2×10^4	0.507	10.93	2.03×10^{-3}	1.11×10^{-3}	0.999
B6	10^5	31	2	B2	A	1.2×10^4	0.343	3.539	5.94×10^{-4}	1.76×10^{-4}	0.194
B7	10^5	31	2	0.1	A	5.1×10^4	0.341	3.503	5.92×10^{-4}	1.75×10^{-4}	0.194
B8	10^6	63	0	0.5	na	3.7×10^3	0.556	22.59	1.60×10^{-4}	1.88×10^{-4}	1.350
B9	10^6	31	0	B4	na	2.2×10^4	0.503	22.08	8.97×10^{-4}	4.72×10^{-4}	0.995
B10	10^6	31	1	B9	D	1.0×10^4	0.469	16.60	5.35×10^{-4}	2.03×10^{-4}	0.501
B11	10^6	31	1	0.1	A	1.0×10^5	0.400	14.18	5.25×10^{-4}	2.02×10^{-4}	0.510
B12	10^6	31	2	0.1	A	1.2×10^5	0.305	7.693	2.73×10^{-4}	7.72×10^{-5}	0.224
B13	10^6	31	2	0.5	A	5.9×10^4	0.308	7.778	2.75×10^{-4}	7.75×10^{-5}	0.223
B14	10^7	63	0	B8	na	4.2×10^4	0.505	45.29	3.82×10^{-4}	1.96×10^{-4}	0.994
B15	10^7	63	2	B15	D	1.3×10^5	0.394	20.62	1.01×10^{-4}	2.93×10^{-5}	0.279
B16	10^7	63	2	0.1	A	1.9×10^5	0.239	11.90	8.54×10^{-5}	2.22×10^{-5}	0.277

† Flow concentrated: A ascending limb; D descending limb; na not applicable.

3 Bottom heating

In this section we discuss what effects increasing the viscosity with depth have on convection when the box is heated from below. One of the objectives of this study is to define the steady-state solution, but, as will become clear, this is often difficult because of the slow approach to steady state in certain instances. In these models the top surface is held at a temperature of 0 and the bottom at 1. Calculations have been carried out at $Ra_T = 10^4$, 10^5, 10^6 and 10^7 and β up to 2 and are summarized in Table 1. We will first briefly review the qualitative features of the constant viscosity case, the so-called Rayleigh–Bénard convection. This case has been systematically investigated by Moore & Weiss (1973), McKenzie *et al.* (1974) and Jarvis & Peltier (1982).

In Fig. 1(a) the constant viscosity case with $Ra_T = 10^6$ (model B8, Table 1) is shown. This type of plot is shown a number of times through this paper. The frames show from top to bottom: the top surface heat flux (Q), contours of the temperature field (T), contours of the stream function ψ (STR), contours of the vorticity ω (VOR), and lastly the horizontal

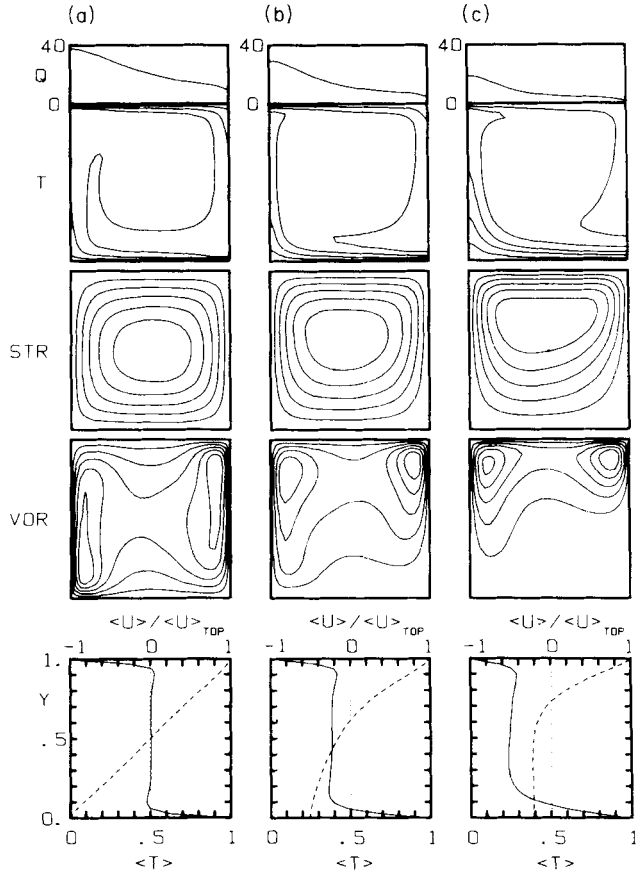

Figure 1. Results for $Ra_T = 10^6$, $\mu = 0$. (a) $\beta = 0$ (model B9). The ranges of the contoured functions, in the form (minimum, maximum) are T: (0, 1), STR: $(-3.27\times10^{-4}, 0)$, VOR: $(0, 8.13\times10^{-3})$; (b) $\beta = 1$ (B12) T: (0, 1), STR: $(-1.37\times10^{-4}, 0)$, VOR: $(0, 5.46\times10^{-3})$; and (c) $\beta = 2$ (B13) T: (0, 1), STR: $(-4.9\times10^{-5}, 0)$, VOR: $(0, 3.13\times10^{-3})$. The quantities shown are surface heat flux (Q), temperature (T), stream function (STR), vorticity (VOR) and the horizontal averages of the horizontal velocity (dashed line) and the temperature (solid line).

averages of the horizontal velocity (dashed line) and the temperature (solid line). The temperature field (Fig. 1a) shows a thin hot limb on the left side of the box rising from the lower boundary layer, while a thin cold limb on the right descends from the top thermal boundary layer. The cold top boundary layer thickens as material moves to the right and this is reflected by a top surface heat flux which decays from the ascending to the descending limb. The two buoyant limbs drive the core of the fluid which remains isothermal. The temperature profile in the lower frame shows that most of the interior has a temperature of 0.5 with large conductive gradients on the top and bottom. From the T profile, we see temperature overshoots just inside the boundary layers (Jarvis & Peltier 1982): a hot overshoot in temperature inside the cold boundary layer and a cold overshoot inside the hot boundary layer. According to Jarvis & Peltier (1982) this is due to the horizontal advection of heat out of the buoyant limbs near the top for the rising limb where the velocities slow and near the bottom for the descending limb.

The stream function for the bottom heated case (Fig. 1a) shows that the flow is essentially symmetric and the strongest velocity gradients occur where the buoyant limbs start descending and ascending into the flow. As the Rayleigh number increases the boundary layers thin, but the core flow remains essentially constant.

In Fig. 2 we show the Nu–Ra_T plot for the calculations summarized in Table 1. The open circles are for the Rayleigh–Bènard convection. The solid line passing through the $\beta = 0$ Nu points is from Jarvis & Peltier (1982) and graphically illustrates the good agreement between the two studies. Jarvis & Peltier (1982) in general used finer grids than used here. To see how reproducible the Nu results are, we bracketed Nu by starting with both a higher and a lower initial temperature. The usual initial temperature was 0.5 which is expected for Rayleigh–Bènard convection in a steady-state. From Table 1, model B3 started with

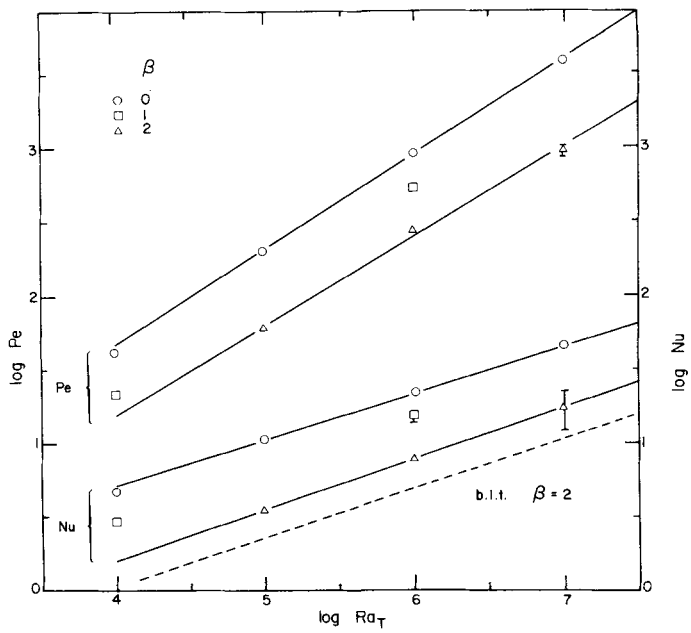

Figure 2. Nu–Ra_T and Pe–Ra_T results for the bottom heated models ($\mu = 0$). The curve drawn through the $\beta = 0$ Nu data points is from Jarvis & Peltier (1982). All other solid lines are linear regressions. The dashed line is from the boundary layer calculations of Londe & Davies (1985).

$\bar{T} = 0.25$, B4 with 0.5 and B5 with 0.75. Both models B4 and B5 have the same Nu of 10.93; B3, however, which was not run for as long as B5 still was warming and its Nu was slowly rising. This re-enforces the notion that the $Nu-Ra_T$ power-law relation for the Rayleigh–Bènard convection is easily reproducible.

The effect of increasing the viscosity with depth is illustrated in Fig. 1 for $Ra_T = 10^6$. The velocities in the lower portions of the convecting region slow and the lower thermal boundary layer thickens. Whereas equal changes in temperature occurred between the top and bottom boundary layers for the uniform viscosity case, most of the temperature changes now occur across the lower boundary layer. Both the bottom and the top boundary layers thicken as they move across the edge of the box. The thickening of the top boundary layer from the ascending to the descending limb is still reflected in the decreasing top surface heat

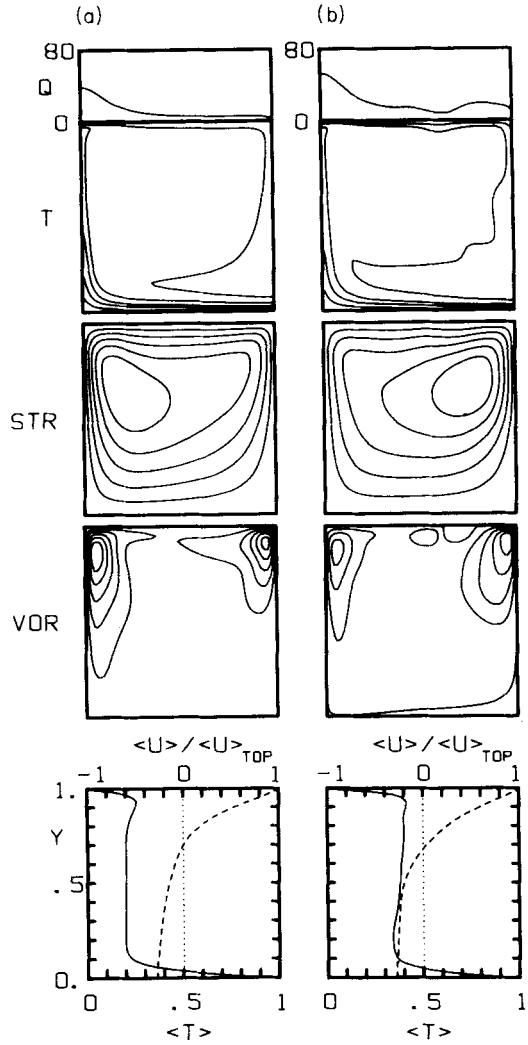

Figure 3. Results for $Ra_T = 10^7$, $\mu = 0$, and $\beta = 2$ for two different initial temperatures. (a) $T_i = 0.1$, the ranges are T: (0, 1), STR: $(-1.48 \times 10^{-5}, 0)$, VOR: $(0, 2.06 \times 10^{-3})$; (b) $T_i = 0.5$, T: (0, 1), STR: $(-2.10 \times 10^{-5}, 0)$, VOR: $(-4.77 \times 10^{-4}, 2.46 \times 10^{-3})$. Otherwise as in Fig. 1.

flux. The ratio between the heat flux on the hot side and that on the cold side is about the same for the β values used (within a factor of 2).

The flow also changes considerably from the symmetric flow characteristic of the constant viscosity case. The most important feature is the concentration of the flow near the top (Torrance & Turcotte 1971a; Houston & De Bremaeker 1975). This is clearly evident in the horizontal velocity profiles shown in the bottom frames of Fig. 1(b, c) (dashed line). Whereas the velocity changed linearly with depth in the constant viscosity case (Fig. 1a), in the $\beta = 1$ case the gradient is greatly reduced in the bottom half. The velocity gradients become large in the top portion as is evident from both the velocity profiles, as well as from the concentration of the vorticity in the top half (Fig. 1c).

There is an important change in the flow pattern, which is subtle at low Ra_T, but at high Ra_T is quite pronounced. For greater viscosity changes the vertical velocities in the ascending portion of the flow become larger than in the descending portion and the streamlines become concentrated in the ascending limb (Londe & Davies 1985). At low Ra the effect is virtually unnoticeable, and Torrance & Turcotte (1971a) did not mention it, although it can be seen in their fig. 2(b). Houston & De Bremaeker (1975) noticed the effect, but said that it was only of minor importance. However, the concentration of buoyancy in the ascending limb, for example at $Ra_T = 10^7$ (Fig. 3a), is quite strong. The centre of circulation is strongly concentrated toward the top of the ascending limb. There are also large velocity gradients in this area as indicated by the vorticity. As discussed by Londe & Davies (1985), as the bottom thermal boundary layer becomes thicker, more of the buoyancy forces tend to be concentrated in the ascending limb. Most of the interior remains isothermal. The combined temperature- and depth-dependent viscosity simulations of Torrance & Turcotte (1971a, b) at high Ra showed a concentration of buoyancy in a narrow hot ascending limb. This points to the value of the simplified calculations presented here, because they show that much of this behaviour is due to the depth dependence of the viscosity and not to the temperature dependence.

Caution must be exercised as to where the buoyancy is concentrated because the calculations did not converge to a steady-state. The flow shown in Fig. 3(a) (with $Ra_T = 10^7$ and $\beta = 2$) started with $\bar{T} = 0.1$ and the fluid warmed to reach this state (Table 1, model B16). We also started from the constant viscosity case at $Ra_T = 10^7$ (model B14) and set $\beta = 2$ so that $\bar{T}$ initially was 0.505 (model B15); in this case the flow was strongly concentrated in the descending portion of the flow (Fig. 3b). Each of the solutions were only changing by small amounts over hundreds of time steps. When the simulations were terminated the Nu between the two cases differed by almost a factor of 2. For the warmer start case Nu = 21 and for the colder start case Nu = 12 (Table 1). At Ra_T below 10^7, however, the Nu closely converged for the warm and cold start models: models B12 and B13 at $Ra_T = 10^6$ (Table 1), for example.

4 Internal heating

In this section the effect of depth-dependent viscosity on an internally heated fluid is explored with calculations at $Ra_q = 10^5, 5 \times 10^5, 10^6, 5 \times 10^6$, and 10^7 and with β taking on values from 0 to 3. Again, as with the bottom heated case all the surfaces are stress free; the bottom heat flux is held constant. Solutions for $Ra_q = 5 \times 10^5$ and 5×10^6 are shown in Figs 4 and 5, respectively.

The constant viscosity case, as studied by McKenzie *et al.* (1974) is described first. The case for $Ra_q = 5 \times 10^5$ is shown in Fig. 4(a). When the fluid is heated entirely from within and the viscosity is constant, the fluid moves upward over a broad area and slowly warms; as

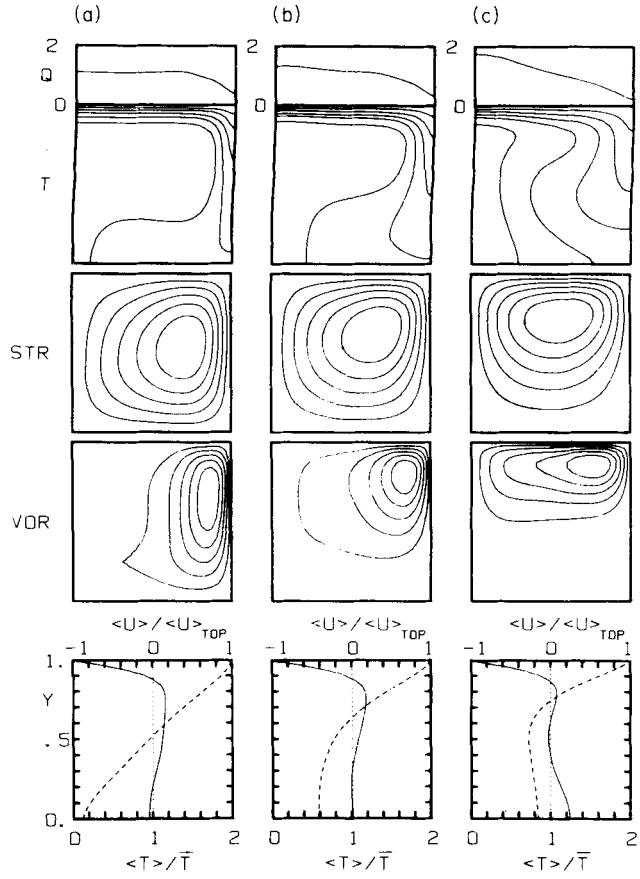

Figure 4. Results for internally heated models $Ra_q = 5 \times 10^5$, $\mu = 1$. (a) $\beta = 0$ (model I4). The ranges are T: (0, 0.093), STR: $(-6.55 \times 10^{-5}, 0)$, VOR: $(0, 2.64 \times 10^{-3})$; (b) $\beta = 1$ (I5), T: (0, 0.1), STR: $(-4.38 \times 10^{-5}, 0)$, VOR: $(0, 1.87 \times 10^{3})$; and (c) $\beta = 2$ (I6) T: (0, 0.13), STR: $(-2.58 \times 10^{-5}, 0)$, VOR: $(-1.74 \times 10^{-6}, 1.18 \times 10^{-3})$. The horizontally averaged temperatures have been normalized by T. Otherwise as in Fig. 1.

it moves near to the surface heat is lost uniformly by conduction (indicated by a fairly constant heat flux and the constant horizontal isotherms across the top). The cold fluid rapidly descends on the right (in Fig. 4a) and the streamlines are centred toward this descending limb. The vorticity is concentrated over the descending limb which indicates large spatial gradients in the velocity there. However, over the broad zone of upwelling there is much less vorticity and this indicates the velocity is more uniform there. This area of uniform velocity is also more isothermal, but not to the same degree as in the bottom heated cases. These phenomena are all dependent on the Rayleigh number: as Ra_q increases the thermal boundary layer thins and the centre of circulation shifts more to the narrow descending limb. The zone of upwelling, which has essentially uniform vertical velocity, increases in size as Ra_q increases. The horizontal velocity, horizontally averaged at each level of the box (dashed line, bottom frame of Fig. 4a), linearly varies with depth for Ra_q at least $>10^5$ and obtains approximately the same velocity on the bottom as on the top (i.e. $\langle U_{BOT} \rangle / \langle U_{TOP} \rangle$ is about 0.9). The horizontally averaged temperature profile (solid line, lower frame Fig. 4a) shows the steep conductive gradient through the top and the approxi-

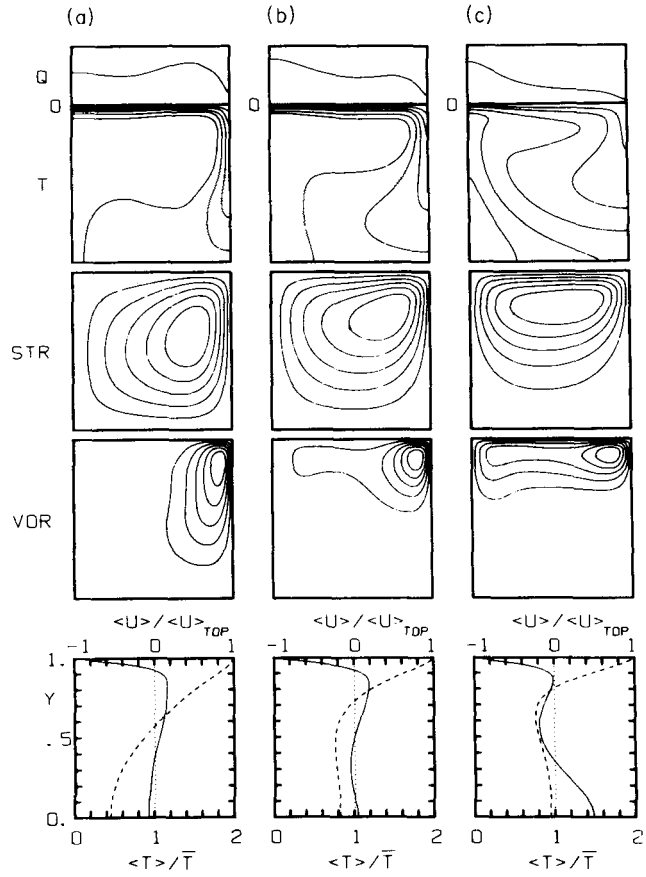

Figure 5. Results for $Ra_q = 5 \times 10^6$, $\mu = 1$. (a) $\beta = 1$ (I11), the ranges are T: (0, 0.067), STR: (-1.26×10^{-5}, 0), VOR: (-2.81×10^{-5}, 8.91×10^{-4}); (b) $\beta = 2$ (I12) T: (0, 0.068), STR: (-7.12×10^{-6}, 0), VOR: (0, 6.88×10^{-4}); (c) $\beta = 3$ (I13), T: (0, 0.10), STR: (-4.34×10^{-6}, 0), VOR: (-1.14×10^{-5}, 4.19×10^{-4}). Otherwise as in Fig. 4.

mately uniform thermal state of the interior. The highest temperatures occur in the interior and not at the bottom as in the Rayleigh–Bènard case. There is a modest decrease in $\langle T \rangle / \bar{T}$ near the bottom and this results from the injection of cold fluid into the bottom from the descending limb.

When a vertical viscosity gradient is introduced (Fig. 4b, c for $Ra_q = 5 \times 10^5$) the velocities in the lower section decrease. The centre of the streamlines shifts upward and they become more horizontally centred. In the constant viscosity case the streamlines were approximately symmetrical about a line passing through at mid-depth. When $Ra_q = 5 \times 10^5$ and $\beta = 1$ (Fig. 4b), for example, the gradient of the counter velocity is greatly reduced and near the bottom the velocity is approximately uniform. There is still a steep velocity gradient (essentially linear) in the top half. When β is increased from 1 to 2, Fig. 4(c) (now a factor of 100 difference in viscosity between the top and bottom surfaces), the horizontally averaged velocity becomes nearly constant through the bottom 3/4 of the box and there is even a slight reverse in the velocity gradient with the largest counter velocity occurring at mid-depth. This is reflected in the concentration of vorticity through the top half. When β is increased still further to 3, for example when $Ra_q = 5 \times 10^6$ (Fig. 5c), the largest counter-

velocities are clearly seen to occur at mid-depth and the velocities become very small at the bottom, i.e. $\langle U_{BOT}\rangle/\langle U_{TOP}\rangle \approx 0.05$ when $Ra_q = 5 \times 10^6$. The depth to which the direction of average horizontal velocity reverses decreases as the viscosity gradient is increased and is only about 0.3 when $\beta = 2$ and 0.2 when $\beta = 3$ at $Ra_q = 5 \times 10^6$. As β increases, the horizontally averaged velocity gradients in the top portion increase while those through the bottom portion decrease. Qualitatively these phenomena vary very little as a function of Rayleigh number; quantitatively $\langle U_{BOT}\rangle/\langle U_{TOP}\rangle$ becomes slightly larger at higher Rayleigh numbers.

As the viscosity gradient increases the width of the thermal limb increases and the centre of the streamlines and vorticity is shifted away from where the descending limb originally was located. When β is increased to 2, the thermal structure becomes distorted, when $Ra_q \leq 10^6$, and the surface heat flux, which was constant across the top at least up to $\beta = 1$, now decreases from the ascending limb to the descending limb. For a large β at a given Ra, for example $\beta = 3$ when $Ra_q = 5 \times 10^6$ (Fig. 5c), the largest horizontally averaged temperatures occur at the lower surface and a conductive thermal gradient is nearly approached as the bottom region approaches conductive stability. Recall that for an internally heated fluid, the conductive temperature profile is parabolic. The thermal structure starts to resemble the top half of the bottom heated case: the top thermal boundary layer thickens with distance across the top and ascending and descending limbs become more equivalent in velocity and velocity gradients (as indicated by the appearance of vorticity in the upwelling region). The fluid slowly moves through the lower 2/3 of the box and warms, but now hot fluid emerges into the lower viscosity upper region and a narrower faster moving upwelling region results. Because much of the heat is generated in the bottom and deposited at the bottom of the lower viscosity region, the top half has attributes making it resemble the Rayleigh–Bènard form of convection.

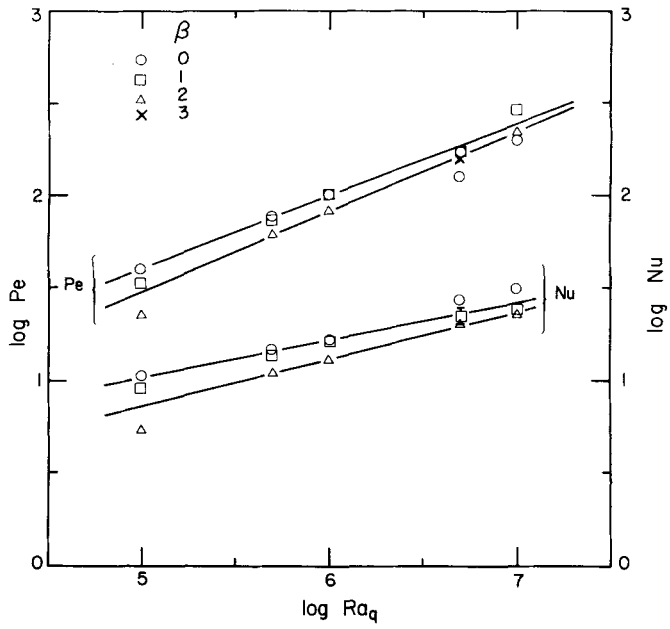

Figure 6. $Nu-Ra_q$ and $Pe-Ra_q$ results for $\mu = 1$. For each set (Nu and Pe) the higher line is a regression for $\beta = 0$ results while the lower is for $\beta = 2$.

Table 2. Summary of runs with bottom heat flux prescribed.

Model	Ra_q	mesh points	β	total flow time	Nu	$\langle U_{TOP} \rangle$	$\tilde{U}$	$\langle U_{BOT} \rangle / \langle U_{TOP} \rangle$
$\mu = 1$								
I1	10^5	31	0	6.9×10^4	10.39	3.99×10^{-4}	2.18×10^{-3}	0.866
I2	10^5	31	1	4.1×10^4	8.97	3.29×10^{-4}	1.32×10^{-4}	0.410
I3	10^5	31	2	1.1×10^5	5.46	2.26×10^{-4}	6.67×10^{-5}	0.160
I4	5×10^5	31	0	1.5×10^5	14.35	1.51×10^{-4}	7.96×10^{-5}	0.883
I5	5×10^5	31	1	8.2×10^4	13.83	1.43×10^{-4}	5.69×10^{-5}	0.425
I6	5×10^5	31	2	7.1×10^4	10.78	1.21×10^{-4}	3.48×10^{-5}	0.161
I7	10^6	31	0	1.7×10^5	16.38	9.72×10^{-5}	5.02×10^{-5}	0.895
I8	10^6	31	1	1.0×10^5	16.24	9.66×10^{-5}	3.84×10^{-5}	0.439
I9	10^6	31	2	2.3×10^5	13.01	8.30×10^{-5}	2.38×10^{-4}	0.164
I10	5×10^6	63	0	3.0×10^5	26.43	2.49×10^{-5}	6.95×10^{-6}	0.461†
I11	5×10^6	63	1	4.7×10^5	22.91	3.38×10^{-5}	1.48×10^{-5}	0.549
I12	5×10^6	63	2	4.5×10^5	19.62	3.40×10^{-5}	9.58×10^{-6}	0.180
I13	5×10^6	63	3	3.7×10^5	12.87	3.18×10^{-5}	6.57×10^{-6}	0.051
I14	10^7	63	0	2.5×10^5	30.31	1.99×10^{-5}	6.42×10^{-6}	0.690†
I15	10^7	63	1	9.7×10^5	24.26	2.81×10^{-5}	1.10×10^{-5}	0.492
I16	10^7	63	2	7.0×10^5	22.68	2.19×10^{-5}	6.22×10^{-6}	0.194
$\mu = 0.5$								
H1	10^7	63	0	3.0×10^5	20.76	2.61×10^{-5}	1.26×10^{-5}	1.209
H2	10^7	63	1	3.6×10^5	18.28	3.14×10^{-5}	1.14×10^{-5}	0.527
H3	10^7	63	2	4.1×10^5	14.05	2.87×10^{-5}	7.88×10^{-6}	0.214

† Aspect ratio of cell (width/depth) was 1/3 for I13 and 1/2 for I14; all others $a = 1$.

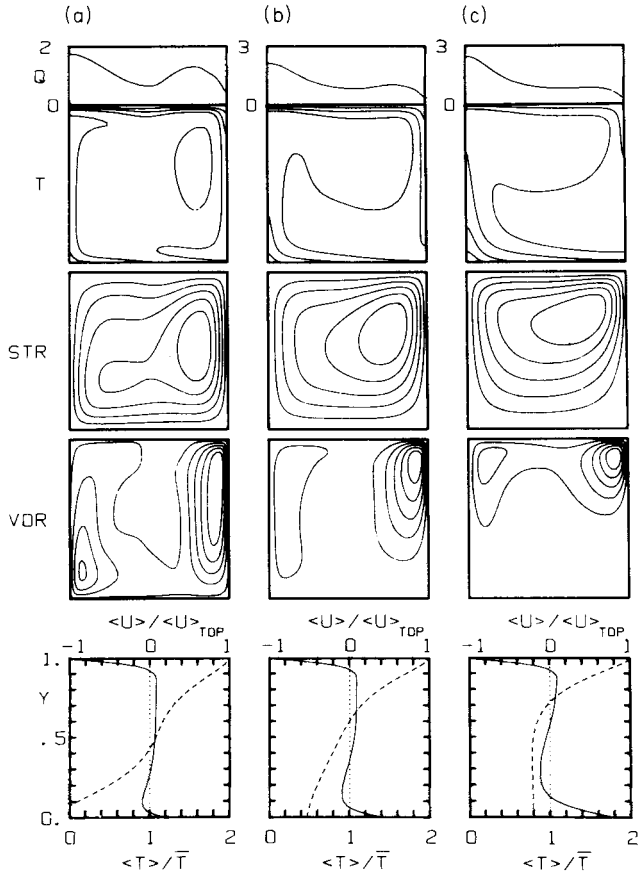

Figure 7. Results for models heated half internally and half from below, $Ra_q = 10^7$, $\mu = 0.5$. (a) $\beta = 0$ (H1) the ranges are T: (0, 0.073), STR: $(-9.36 \times 10^{-6}, 0)$, VOR: $(-9.72 \times 10^{-5}, 7.29 \times 10^{-4})$; (b) $\beta = 1$ (H2) T: (0, 0.093), STR: $(-8.61 \times 10^{-6}, 0)$, VOR: $(0, 6.61 \times 10^{-4})$; and (c) $\beta = 2$ (H3) T: (0, 0.13), STR: $(-5.35 \times 10^{-6}, 70)$, VOR: $(0, 5.18 \times 10^{-4})$. Otherwise as in Fig. 4.

5 Half bottom and half internally heated

The true heating mode driving mantle convection must lie between the two scenarios just considered: bottom heated and internally heated. For completeness we have made a sequence of calculations at $Ra_q = 10^7$ with half the heat being generated internally and half being conducted through the bottom boundary (i.e. $\mu = 0.5$); the bottom heat flux was held constant. The degenerate case of $\beta = 0$ (constant viscosity) was studied at a number of Ra by McKenzie *et al.* (1974). Our results are summarized in Table 2 and displayed in Fig. 7.

The constant viscosity case is shown in Fig. 7(a). This simulation did not converge to a steady state; Nu still was exhibiting small oscillations at various frequencies with amplitudes of about 10 per cent of the total magnitude. The solution contains features seen in both the bottom and internally heated cases. The core flow is driven by both the ascending and descending thermal limbs, but the descending limb has more than half of the buoyancy. At this Ra, the top boundary layer is exhibiting time dependence as indicated by the down-warping of the top thermal boundary layer in the middle and this is indicated by the valley in the surface heat flux. The horizontally averaged temperature profile in the last frame of Fig. 7(a) shows the isothermal state of the interior as well as a larger thermal drop across the top boundary than across the bottom. The flow still is concentrated in the descending limb.

When a vertical viscosity gradient is introduced, the slower velocities result in an increasing temperature change across the lower thermal boundary layer. When β is as large as 2, the average temperature profile ($\langle T \rangle / \bar{T}$) is qualitatively similar to a lower Ra simulation with bottom heating. However, this increased buoyancy in the ascending region on the left is not yet as large as on the right and the parameter μ must be less than at least 0.5 (and perhaps very close to 0) for the depth dependence to result in the concentration of flow in the ascending region.

6 Rayleigh number scaling

In this section the dependence of the dimensionless heat flux (Nusselt number) and convective velocities (Peclet number) on Rayleigh number are summarized. These scaling relations are important for a number of reasons. The Nusselt number summarizes the heat transport efficiency of the convective flow; if vastly different efficiencies were found between the constant viscosity and variable viscosity types of convection, then this would point to a need for additional thermal history modelling using parameterized convection models. For convection models where the top surface velocity is prescribed (cf. Lux 1978; Davies 1986) in order to simulate the kinematic features of plate motion, Pe–Ra scaling is important. The scaling is used to maintain the same ratio of boundary driven to buoyancy driven forces in the numerical models (run at Ra_q 10^5–10^6, Davies 1986) compared to the real mantle, which may have $Ra_q \sim 10^9$.

The Nusselt and Peclet number results are summarized in Fig. 2 for the bottom heated cases ($\mu = 0$) and in Fig. 6 for the internally heated cases ($\mu = 1$) and are shown with curves of the form

$$Nu = b\, Ra_T^c = b' Ra_q^{c'} \tag{24}$$

$$Pe = d\, Ra_T^e = d' Ra_q^{e'}. \tag{25}$$

The parameters of the curves are summarized in Table 3. No curve has been drawn through the $\beta = 1$ cases. From Fig. 2 it is clear that only the coefficients b and d have changed significantly and the slopes c and e have remained essentially constant. This was predicted from the boundary layer work of Londe & Davies (1985). For the $\mu = 0$ simulation there is a

Table 3. Pe–Ra, Nu–Ra results.

μ	β	b (or b')	c (or c')	d (or d')	e (or e')	regression limits
0	0	0.313	0.309	0.130	0.639	10^5 to 10^7
0	2	0.065	0.347	0.063	0.599	10^5 to 10^7
1	0	1.061	0.198	0.456	0.389	10^5 to 10^6
1	2	0.408	0.250	0.210	0.432	5×10^5 to 10^7

65 per cent decrease in the efficiency of heat transport between the constant viscosity case ($\beta = 0$) and $\beta = 2$ at $Ra_T = 10^6$. However, for the simulations that were entirely internally heated, the decrease in efficiency was 20 per cent (at $Ra_q = 10^6$). The different changes in heat transport efficiency between the $\mu = 0$ and 1 models is significant. For the $\mu = 0$ case heat enters only through the lower boundary where the viscosity is highest, and the transport of this heat away from this boundary is reduced. The effect in the $\mu = 1$ cases is less drastic because now the heat is generated uniformly through the box and only a small fraction of the heat transport is reduced.

The changes in Peclet number between the $\mu = 0$ and 1 cases for different β is interpreted in terms of changes in the efficiency of heat transport. For $\mu = 0$, Pe decreased by 70 per cent from $\beta = 0$ to 2 while for $\mu = 1$ there was a 15 per cent decrease at $Ra = 10^6$ and this is close to the values found for Nu. The slopes found at the different β values varied slightly (as can be clearly seen in Fig. 6) but these variations are not significant because of the time dependence of the solutions at Ra_T (and Ra_q) $> 10^6$.

For these calculations we have documented the changes in the horizontal velocity with the viscosity variation. In Fig. 8, the ratio $\langle U_{BOT} \rangle / \langle U_{TOP} \rangle$ is plotted against β. The points plotted are either the result of a single calculation or averages of calculations made with

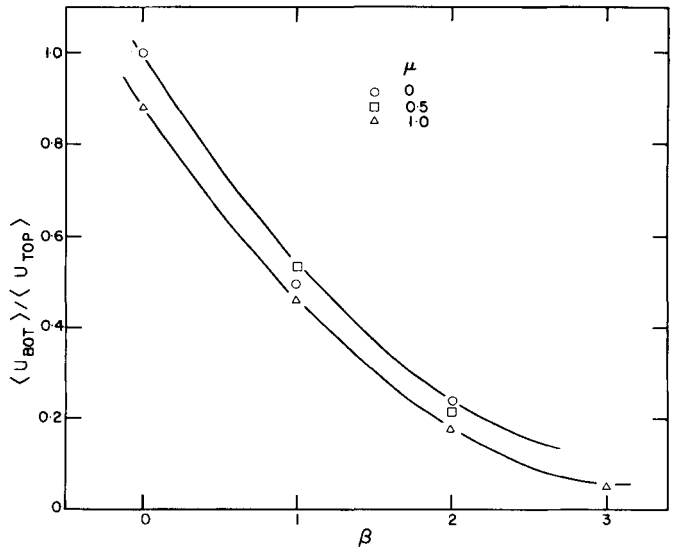

Figure 8. Reduction in the horizontal bottom velocity (normalized by the top velocity) as a function of viscosity variation. β is defined from equation (12) ($\eta = 10^{\mu(1-\gamma')}$). The solid curves bracket the range of velocity ratios obtained. Only cases which resulted in convection cells with an aspect ratio of unity have been plotted.

different initial conditions (Tables 1 and 2). Only flows with aspect ratio 1 have been plotted. There are only slight differences in $\langle U_{BOT} \rangle / \langle U_{TOP} \rangle$ for the different heating modes and the curves shown in Fig. 8 are only drawn to highlight the trend of the results.

7 Discussion

The purpose of these calculations is systematically to investigate the basic flow properties of thermal convection in a medium with a viscosity increasing with depth. These simple models provide the necessary background needed to understand more realistic models of mantle convection where depth-dependence is just one component of multi-parameter viscosity relations. The hypothesis that the viscosity of the mantle may increase with depth has been discussed for about two decades, and was originally prompted by rheological understanding of presumed mantle materials (McKenzie 1967; Weertman 1976). Because of the pressure dependence of thermally activated creep, the viscosity of the mantle may increase with hydrostatic pressure. Discussion of various mantle viscosity distributions seems to have diminished since the work of Cathles (1975) and Peltier & Andrews (1976) on global models of the rebounding surface of the Earth following the last ice age. Cathles and Peltier & Andrews concluded that the Earth's mantle has an approximately uniform Newtonian viscosity throughout. We are not questioning the validity of these studies, but only pointing out that moderate variations in mantle viscosity, which are still allowable from these types of viscosity constraints, may lead to changes in mantle flow.

Recently, Davies (1984) and Hager (1984) have independently suggested that the viscosity of the Earth's mantle may increase with depth by one to two orders of magnitude. Hager (1984) concluded that the lower mantle may have a viscosity about 30 times greater than the upper in order that the positive geoid anomalies observed over trenches be explained by subducted slabs. If the viscosity is greater at depth, then the deformation of the Earth's surface which leads to a negative geoid anomaly, is reduced, and the positive anomaly of the cold slab dominates the geoid signature. Davies (1984) has also suggested a more viscous deep mantle in order to reconcile convective mixing with the longevity of the isotopic heterogeneity of some oceanic islands from the observed ratios of ^{129}Xe isotopes (Allègre *et al.* 1983). If hot spots do arise from chemically and isotopically heterogeneous blobs entrained in mantle flow, then low convective velocities in the deep mantle are consistent with low hot-spot velocities. Low convective velocities in the deep mantle are consistent with, but do not prove, higher viscosities in the deep mantle.

Plate velocities in different reference frames are about 5 cm yr^{-1} and up to about 10 cm yr^{-1} for oceanic plates and 1–2 cm yr^{-1} for continental plates (Kaula 1975; Chase 1978). At times, however, the continental plates may have velocities of up to 7 cm yr^{-1} (Schultz & Gordon 1984). If the hot-spots migrate with respect to each other, then they do so with velocities less than oceanic plates (Morgan 1972). There have been a number of studies which have tried to estimate the relative velocity between the hot-spots (Molnar & Atwater 1973; Burke, Kidd & Wilson 1973; Molnar & Francheteau 1975), but the results were inconclusive. Recently the problem has been addressed again by Chase & Sprowl (1984) and they concluded that some hot-spots may move coherently as groups with velocities of 1–7 cm yr^{-1}. The problem with estimating velocities of hot-spots is that the errors associated with plate histories (based on magnetic lineations and transform fault orientation) are significant (Stock & Molnar 1983) and the (possibly ?) slow moving hot-spots may not yet be resolved above these errors. But the evidence is suggestive, and it seems quite plausible that some hot-spots may move with velocities of about 1/5 to 1/10 of the surface flow of convection, that is, of the plates. In Fig. 8 we see the reduction in

convective velocity on the bottom of the box with respect to the top as a function of viscosity variation. From the results of Hager (1984) the value of β may possibly be less than 2 (Hager used a step-function viscosity distribution and the result is not exactly applicable); from Fig. 8 the velocity ratios are hence greater than 0.2. Thus, if hot-spots (also the OIB) are derived from sources entrained in lower mantle flow and the viscosity is similar to that suggested by Hager, then the calculated and inferred velocities of the hot spots are about the same. The results are suggestive and more work along these lines is definitely needed.

References

Allegrè, C. J., Brevart, O., Duprè, B. & Minster, J.-F. 1980. Isotopic and chemical effects produced in a continuously differentiating convecting earth mantle, *Phil. Trans. R. Soc. A*, **297**, 447–477.

Allegrè, C. J., Staudacher, T., Sarda, P. & Kurtz, M., 1983. Constraints on the evolution of the earth's mantle from rare gas systematics, *Nature*, **303**, 762–766.

Burke, K., Kidd, W. S. F. & Wilson, J. T., 1973. Relative and latitudinal motion of Atlantic hot spots, *Nature*, **245**, 133–137.

Cathles, L. M., 1975. *The Viscosity of the Earth's Mantle*, Princeton University Press.

Chase, C. G., 1978. Plate kinematics: the Americas, East Africa, and the rest of the world, *Earth planet. Sci. Lett.*, **37**, 355–368.

Chase, C. G. & Sprowl, D. R., 1984. Proper motion of Pacific-plate hot spots, *Eos, Trans. Am. Geophys. Un.*, **65**, 193.

Christensen, U., 1983. Convection in a variable viscosity fluid: Newtonian versus power-law rheology, *Earth planet Sci. Lett.*, **64**, 153–162.

Christensen, U., 1984. Convection with pressure- and temperature-dependent non-Newtonian rheology, *Geophys. J. R. astr. Soc.*, **77**, 343–384.

Creager, K. C. & Jordon, T. H., 1984. Slab penetration into the lower mantle, *J. geophys. Res.*, **89**, 3031–3049.

Davies, G. F., 1977. Whole mantle convection and plate tectonics, *Geophys. J. R. astr. Soc.*, **49**, 459–486.

Davies, G. F., 1984. Geophysical and isotopic constraints on mantle convection: an interim synthesis, *J. geophys. Res.*, **89**, 6017–6040.

Davies, G. F., 1986. Mantle convection under simulated plates: effects of heating modes and ridge and trench migration, and implications for the core–mantle boundary, bathemetry, the geoid and Benioff zones, *Geophys. J. R. astr. Soc.*, **84**, 153–183.

Hager, B. H., 1984. Subducted slabs and the geoid: constraints on mantle rheology and flow, *J. geophys. Res.*, **89**, 6003–6016.

Hager, B. H. & O'Connell, R. J., 1979. Kinematic models of large-scale flow in the earth's mantle, *J. geophys. Res.*, **84**, 1031–1048.

Hofmann, A. W., 1984. Geochemical mantle models, *Terra Cognita*, **4**, 1031–1048.

Houston & De Bremaeker, 1975. Numerical models of convection in the upper mantle, *J. geophys. Res.*, **80**, 742–751.

Jarvis, G. T. & Peltier, W. R., 1982. Mantle convection as a boundary layer phenomenon, *Geophys. J. R. astr. Soc.*, **68**, 385–424.

Jordan, T. H., 1977. Lithospheric slab penetration into the lower mantle, *J. Geophys.*, **43**, 473–496.

Kaula, W. M., 1975. Absolute motions by boundary velocity minimizations, *J. geophys. Res.*, **80**, 244–248.

Landau, L. D. & Lifshitz, E. M., 1959. *Fluid Mechanics*, Pergamon Press, New York.

Londe, M. D. & Davies, G. F., 1985. The application of boundary layer theory to the convective flow of a fluid with a depth dependent viscosity, *Phys. Earth planet. Int.*, **41**, 78–91.

Lupton, J. E. & Craig, H., 1975. Excess ^{3}He in oceanic basalts: evidence for terrestrial primordial helium, *Earth planet. Sci. Lett.*, **26**, 133–139.

Lux, R. A., 1978. The effect of a moving lithospheric plate on convection in the earth's mantle, *PhD dissertation*, The University of Rochester, Rochester, New York.

McKenzie, D. P., 1967. The viscosity of the mantle, *Geophys. J. R. astr. Soc.*, **14**, 297–305.

McKenzie, D. P., Roberts, J. M. & Weiss, N. O., 1974. Convection in the earth's mantle: towards a numerical simulation, *J. Fluid Mech.*, **62**, 465–538.

Molnar, P. & Atwater, T., 1973. The relative motion of hot-spots in the mantle, *Nature*, **246**, 288–291.

Molnar, P. & Francheteau, J., 1975. The relative motion of 'hot spots' in the Atlantic and Indian oceans during the Cenozoic, *Geophys. J. R. astr. Soc.*, **43**, 763–774.

Moore, D. R. & Weiss, N. O., 1973. Two-dimensional Rayleigh-Bènard convection, *J. Fluid Mech.*, **58**, 289–312.

Morgan, W. J., 1972. Plate motions and deep mantle convection, *Mem. geol. Soc. Am.*, **132**, 7–22.

Peltier, W. R. & Andrews, J. T., 1976. Glacial-isotatic adjustment – I. The forward problem, *Geophys. J. R. astr. Soc.*, **46**, 605–646.

Schultz, F. R. & Gordan, R. G., 1984. Root mean square velocities of the continents with respect to the hot spots since the early Jurassic, *J. geophys. Res.*, **89**, 1789–1800.

Stock, J. M. & Molnar, P., 1983. Some geometrical aspects of uncertainties in combined plate reconstructions, *Geology*, **11**, 697–701.

Sweet, R., 1974. A generalized cyclic reduction algorithm, *SIAM J. Numer. Anal.*, **11**, 506–520.

Torrance, K. E. & Turcotte, D. L., 1971a. Thermal convection with large viscosity variations, *J. Fluid Mech.*, **47**, 113–125.

Torrance, K. E. & Turcotte, D. L., 1971b. Structure of convection cells in the mantle, *J. geophys. Res.*, **76**, 1154–1161.

Weertman, J., 1976. The creep strength of the earth's mantle, *Rev. Geophys. Space Phys.*, **8**, 145–168.